nature materials

Article

https://doi.org/10.1038/s41563-023-01620-2

Handedness anomaly in a non-collinear antiferromagnet under spin–orbit torque

Received: 3 January 2023

Accepted: 23 June 2023

Published online: 03 August 2023

Check for updates

Ju-Young Yoon[1,2,3,10], Pengxiang Zhang[3,10], Chung-Tao Chou[3,4], Yutaro Takeuchi[5], Tomohiro Uchimura[1,2], Justin T. Hou[3], Jiahao Han[1] ✉, Shun Kanai[1,2,5,6,7], Hideo Ohno[1,2,5,6,8], Shunsuke Fukami[1,2,5,6,8,9] ✉ & Luqiao Liu[3] ✉

Non-collinear antiferromagnets are an emerging family of spintronic materials because they not only possess the general advantages of antiferromagnets but also enable more advanced functionalities. Recently, in an intriguing non-collinear antiferromagnet Mn_3Sn, where the octupole moment is defined as the collective magnetic order parameter, spin–orbit torque (SOT) switching has been achieved in seemingly the same protocol as in ferromagnets. Nevertheless, it is fundamentally important to explore the unknown octupole moment dynamics and contrast it with the magnetization vector of ferromagnets. Here we report a handedness anomaly in the SOT-driven dynamics of Mn_3Sn: when spin current is injected, the octupole moment rotates in the opposite direction to the individual moments, leading to a SOT switching polarity distinct from ferromagnets. By using second-harmonic and d.c. magnetometry, we track the SOT effect onto the octupole moment during its rotation and reveal that the handedness anomaly stems from the interactions between the injected spin and the unique chiral-spin structure of Mn_3Sn. We further establish the torque balancing equation of the magnetic octupole moment and quantify the SOT efficiency. Our finding provides a guideline for understanding and implementing the electrical manipulation of non-collinear antiferromagnets, which in nature differs from the well-established collinear magnets.

Antiferromagnets have been enthusiastically pursued as new candidate materials in nanoscale spintronic devices because of their immunity to external perturbation and potentials for reaching high storage densities and fast operational speed[1–4]. Non-collinear antiferromagnets represented by Mn_3X (X = Sn, Ge, and so on) are particularly interesting since they not only possess the advantages of conventional antiferromagnets but also exhibit exotic properties from their topological band structures such as large anomalous Hall, anomalous Nernst and magneto-optical Kerr effects, which provide useful mechanisms for detecting the antiferromagnetic states[5–10]. Meanwhile, spin–orbit torque (SOT)[11–13] manipulation of the non-collinear antiferromagnetic spin structure has been successfully demonstrated in

[1]Laboratory for Nanoelectronics and Spintronics, Research Institute of Electrical Communication, Tohoku University, Sendai, Japan. [2]Graduate School of Engineering, Tohoku University, Sendai, Japan. [3]Department of Electrical Engineering and Computer Science, Massachusetts Institute of Technology, Cambridge, MA, USA. [4]Department of Physics, Massachusetts Institute of Technology, Cambridge, MA, USA. [5]WPI-Advanced Institute for Materials Research, Tohoku University, Sendai, Japan. [6]Center for Science and Innovation in Spintronics, Tohoku University, Sendai, Japan. [7]Division for the Establishment of Frontier Sciences of Organization for Advanced Studies, Tohoku University, Sendai, Japan. [8]Center for Innovative Integrated Electronic Systems, Tohoku University, Sendai, Japan. [9]Inamori Research Institute for Science, Kyoto, Japan. [10]These authors contributed equally: Ju-Young Yoon, Pengxiang Zhang. ✉e-mail: jiahao.han.c8@tohoku.ac.jp; s-fukami@riec.tohoku.ac.jp; luqiao@mit.edu

https://doi.org/10.1038/s41563-023-01620-2

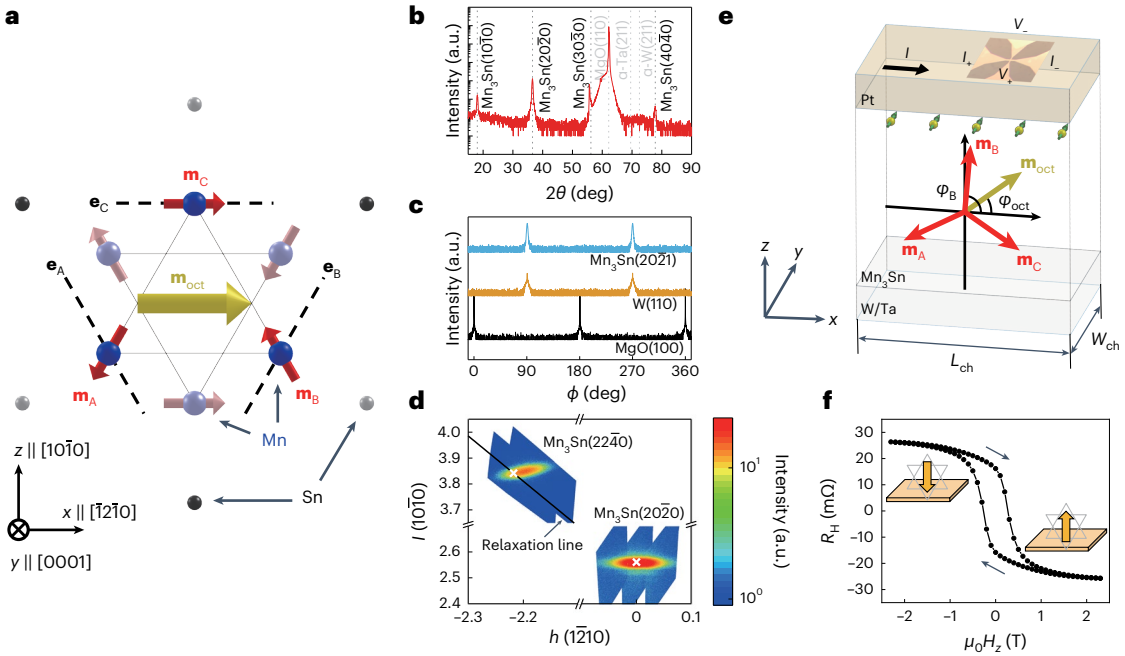

Fig. 1 | Structural and transport properties in W(2 nm)/Ta(3 nm)/Mn_3Sn (8.8 nm)/Pt(5 nm) stacks deposited on MgO(110) substrate. a, Schematics for the crystal and magnetic structure of $D0_{19}$-Mn_3Sn. Blue and black spheres represent Mn and Sn atoms, respectively. The red and yellow arrows represent the magnetic moments of Mn atoms and the octupole moment, respectively. The blurred colours denote the atoms and magnetic moments in neighbouring kagome planes. The black dashed lines represent the magnetic easy axes of individual sublattice moments towards neighbouring Sn atoms. **b**,**c**, X-ray diffraction patterns of the out-of-plane 2θ–θ scan (**b**) and in-plane ϕ scan (**c**). **d**, The reciprocal space map near the Mn_3Sn $(22\bar{4}0)$ and $(20\bar{2}0)$ peaks. The white cross marks represent the theoretical positions calculated using the lattice constant obtained from the $Mn_3Sn(20\bar{2}0)$ peak. The relaxation line indicates the position when the strain is fully relaxed. The centre of the $(22\bar{4}0)$ peak is located to the right of the relaxation line, indicating a tensile strain along $[\bar{1}2\bar{1}0]$. **e**, Schematic of the transport measurement. The in-plane spins (yellow spheres and green arrows) are injected from Pt to Mn_3Sn. The sublattice moments and the octupole moment are defined as $\mathbf{m}_{(A,B,C)}$ and $\mathbf{m}_{oct}$ with angles of $\varphi_{(A,B,C)}$ and φ_{oct}, respectively. An optical micrograph of the fabricated Hall bar with a channel width W_{ch} and a length L_{ch} of 15–30 μm and 90 μm, respectively, is shown on the top of the stacks with the definition of the current and voltage directions. **f**, R_H as a function of the out-of-plane field H_z measured at I = 5 mA. The inset schematic illustrates the orientation of the octupole moment.

experiments such as chiral-spin rotation[14,15] and switching[16–19]. In the existing studies, an octupole moment (Fig. 1a) has been introduced to represent the collective magnetic order of non-collinear antiferromagnets[20,21], playing a similar role to the overall magnetic order parameters (magnetization vector or Néel vector) in collinear magnets (ferromagnets, collinear ferrimagnets and antiferromagnets). When a damping-like (DL) SOT is applied onto collinear magnets, the overall magnetic order parameter undergoes the same precession handedness as that of individual moments[22–26]. Following this configuration, it has been conceived that the SOT-driven dynamics of the octupole moment in a non-collinear antiferromagnet can be understood in a similar way and thus undergo the same handedness as that in collinear magnets. However, this is a crucial speculation waiting to be examined. Moreover, a quantification of the SOT in non-collinear antiferromagnets is still missing, which further hampers the fundamental understanding of the SOT-driven dynamics and the prospect of building efficient spintronic devices.

In this work, by probing the SOT-driven octupole moment reversal in a non-collinear antiferromagnet Mn_3Sn and extracting the intermediate states of the octupole moment from a.c. second-harmonic and d.c. measurements, we demonstrate that the octupole moment rotates under the DL SOT with an opposite handedness to that of individual moments, leading to a SOT switching polarity opposite to that of collinear magnets. We call this phenomenon, which is missing in previous studies, the 'handedness anomaly', and it is a unique effect stemming from the interplay between the SOT and the chiral-spin structure of Mn_3Sn. We also find that efficient, deterministic SOT switching takes place only when injected spins are along a direction out of the magnetic easy plane. In the optimal configuration, we establish the torque balancing equation of the octupole moment, verifying that the octupole moment is not a misleading picture but a rigorous concept to reveal the SOT dynamics of non-collinear antiferromagnets. The developed experimental methods and theoretical framework provide a platform for understanding and controlling the dynamics of the magnetic order in non-collinear antiferromagnets.

Structural and transport properties of epitaxially grown Mn_3Sn thin films

We use $D0_{19}$-Mn_3Sn for our experiment, which is a representative non-collinear antiferromagnet with a hexagonal $D0_{19}$ structure in the space group $P6_3/mmc$. As shown in Fig. 1a, the Mn atoms form a kagome lattice with their magnetic moments oriented in a triangular configuration in the magnetic easy plane (0001). The spin orientations of three sublattices A, B and C form an angle of ~120° with a fixed chirality determined by the Dzyaloshinskii–Moriya interaction[27–29]. Because of the intrinsic magnetic anisotropy from individual sublattice moments, Mn_3Sn also exhibits a very small uncompensated net moment $\mathbf{m}_{net} = \mathbf{m}_A + \mathbf{m}_B + \mathbf{m}_C$, providing a useful handle for controlling the antiferromagnetic order with external magnetic fields[27,28,30].

We deposit Mn_3Sn films on MgO(110) substrate by sputtering (Methods). The stacks consist of W(2 nm)/Ta(3 nm)/Mn_3Sn(8.8 nm)/Pt(5 nm) from the substrate side. Using single-crystal MgO as a template and W and Ta as seeding layers[31,32], we obtain a $(10\bar{1}0)$ Mn_3Sn thin film with its magnetic easy plane (0001) oriented perpendicular to the sample surface. This configuration allows us to inject in-plane spins via the spin Hall effect to control the antiferromagnetic order in the

easy plane[33,34], and to get a large anomalous Hall voltage by using the Berry curvature in the k_x–k_y plane in the momentum space[35,36]. The X-ray diffraction pattern of the stack is shown in Fig. 1b, where only the $(10\bar{1}0)$, $(20\bar{2}0)$, $(30\bar{3}0)$ and $(40\bar{4}0)$ peaks of Mn_3Sn are observed, consistent with the expected film growth direction. In addition, 180° periodic peaks are observed for the Mn_3Sn, W and MgO substrate in the in-plane ϕ scan (Fig. 1c), confirming the epitaxial relation of MgO(110)[001] || W(211)[01$\bar{1}$] || $Mn_3Sn(10\bar{1}0)[0001]$. The reciprocal space map shown in Fig. 1d indicates a tensile strain along the $[\bar{1}2\bar{1}0]$ direction, consistent with a previous report[18]. This distortion of the equilateral triangle crystal structure within the kagome plane (Fig. 1a) induces an extra magnetic anisotropy, which is reflected in our measurement of SOT as discussed later.

After patterning the film into Hall bar devices (Fig. 1e), we measure the Hall resistance as a function of the out-of-plane magnetic field (Fig. 1f), where a clear hysteresis loop is observed with a negative anomalous Hall coefficient under the current and voltage directions defined in Fig. 1e, consistent with the intrinsic anomalous Hall effect from the topological semimetallic phase of Mn_3Sn as reported earlier[5–7,31,32]. Here we note that although a very small net moment $\mathbf{m}_{net}$ provides a useful handle for magnetically controlling the antiferromagnetic order, it does not correspond to a magnetic order parameter describing the anomalous Hall state in non-collinear antiferromagnets[5]. On the other hand, the octupole moment $\mathbf{m}_{oct}$, which originates from the symmetry of the chiral magnetic order[20,21] (Supplementary Discussion 1.1), has been adopted as the magnetic order parameter to precisely describe the anomalous Hall state of Mn_3Sn through[16] $R_H(\varphi_{oct}) = R_0 m_{oct,z} = R_0 \sin\varphi_{oct}$, where R_0 is the anomalous Hall coefficient and φ_{oct} is the angle of $\mathbf{m}_{oct}$ (Fig. 1e). Meanwhile, it is known that in the weak anisotropy limit the direction of $\mathbf{m}_{oct}$ is largely parallel to $\mathbf{m}_{net}$, so that $\mathbf{m}_{oct}$ almost follows the applied field under the Zeeman interaction (Supplementary Discussions 1.1 and 1.2). In this sense, the octupole moment of a non-collinear antiferromagnet plays a similar role to the magnetization vector of a regular ferromagnet.

Anisotropy and polarity in the SOT switching of Mn_3Sn

We consider the current-induced dynamics of the magnetic order in Mn_3Sn through the SOT effect. As shown in Fig. 1e, in-plane spins are injected into Mn_3Sn from the top Pt layer via the spin Hall effect. Although the bottom W/Ta layers also inject spins with the same orientation as Pt into Mn_3Sn owing to their opposite signs of spin Hall angle[22,37], we mostly focus on the Pt layer as the major spin current source because of the much smaller resistivity of Pt (Methods). Figure 2a,b shows two measurement configurations, where spins are injected either perpendicular to or lying within the magnetic easy plane, respectively. Under the injected spin current, the DL SOT[38,39] acting on the individual sublattice moments in Mn_3Sn yields effective fields of $\mathbf{H}_{DL}^{(A,B,C)} \propto \mathbf{m}_{(A,B,C)} \times \boldsymbol{\sigma}$ as shown in the figures. According to this picture, the SOT causes different actions on the sublattice moments, when the relative orientations between the injected spin and the crystal orientation differ. For the configuration shown in Fig. 2a, DL torques $\boldsymbol{\tau}_{DL}^{(A,B,C)} \propto -\mathbf{m}_{(A,B,C)} \times \mathbf{H}_{DL}^{(A,B,C)}$ are identically applied to all the three individual sublattice moments with the same direction. In this configuration, the SOT only needs to overcome the weak magnetic anisotropy in the easy plane, which we term the 'easy configuration'. On the other hand, for the configuration shown in Fig. 2b, not only the magnitude but also the direction of the applied DL torque differs between the individual sublattice moments, resulting in a destructive summation of SOT. Furthermore, the SOT needs to overcome a large effective easy-plane magnetic anisotropy, and hence this corresponds to a 'hard configuration'. Here, we do not illustrate the influence of the field-like torques[40] as they do not lead to switching in either configuration (Supplementary Discussion 2).

To switch the antiferromagnetic order, we apply a 100 ms pulse current I in the two configurations of Fig. 2a,b with an external magnetic field along the current direction, similar to the SOT switching of ferromagnets with a perpendicular easy axis[38,39]. We see that bidirectional SOT switching is clearly observed in the easy configuration with a threshold current density $J_{C0} \approx 15\,MA\,cm^{-2}$ (Fig. 2c), where the temperature rises by ~4 K owing to Joule heating, which is low enough to exclude thermally dominated switching (Supplementary Discussion 3). Compared with the field-induced case, the current-induced switching corresponds to about ~30% of the total domains, which may be due to the tilting of the octupole moment by the bias in-plane field and/or the non-perfect perpendicular magnetic anisotropy[15–17,19] and the non-uniform current distribution at the Hall cross[41]. This can be improved by optimizing the magnitude of the in-plane field and device structures, which is not the main focus of this study. In the hard configuration, no obvious SOT switching has been realized over the applied current density range that is more than twice as large as the easy configuration (Fig. 2d).

In the SOT switching of ferromagnets with a perpendicular easy axis, the switching polarity is determined by the direction of the bias field regarding the current direction, which breaks the symmetry in response to the SOT effective field via the Zeeman interaction[38,39]. Since non-collinear antiferromagnets also exhibit a small uncompensated net moment that largely lies parallel to the octupole moment, an identical protocol seems reasonable for the bipolar switching. However, by comparing the SOT switching in Fig. 2c with a W/CoFeB/MgO control sample in Fig. 2e (after considering the different anomalous Hall coefficients in Fig. 1f and the inset of Fig. 2e), we find opposite switching polarities in Mn_3Sn and CoFeB; that is, under the same spin injection conditon[22,37], for example, $+I_x \parallel +H_x$, the SOT in Mn_3Sn and CoFeB effectively acts as a negative and positive, respectively, magnetic field to switch the octupole moment and magnetization vector, respectively, as indicated schematically in Fig. 2f. Such an anomaly in Mn_3Sn indicates that the octupole moment of Mn_3Sn does not react to the applied SOT in complete analogy with the magnetization vector of a ferromagnet. Rather, it suggests that the SOT-induced rotation of the octupole moment, an assembled order parameter, may possess a distinct handedness with respect to that of the individual moments, which will be investigated in subsequent sections.

Magnetic anisotropy in a strained Mn_3Sn thin film

To gather a deeper understanding of the SOT-driven dynamics in Mn_3Sn, we first build a comprehensive relationship between the octupole moment and the applied magnetic field by characterizing R_H as a function of the applied field angles β and γ, as defined in Fig. 2a,b. The blue and black circles in Fig. 3a show typical first-harmonic Hall resistances $R_H^{\omega}(\beta)$ and $R_H^{\omega}(\gamma)$ measured in the easy and hard configurations, respectively. As discussed earlier, since $\mathbf{m}_{oct}$ roughly follows $\mathbf{m}_{net}$, the close-to-sinusoidal line shape of $R_H(\beta)$ reflects the field control of $\mathbf{m}_{oct}$ through $\mathbf{m}_{net}$.

When only considering the intrinsic uniaxial anisotropy for each atomic site in the Mn–Sn bond direction (black dashed lines in Fig. 1a, labelled as $\mathbf{e}_{(A,B,C)}$), $E_{an1} = -K_1\left((\mathbf{e}_A \cdot \mathbf{m}_A)^2 + (\mathbf{e}_B \cdot \mathbf{m}_B)^2 + (\mathbf{e}_C \cdot \mathbf{m}_C)^2\right)$, the antiferromagnet will exhibit a weak, sixfold anisotropy for $\mathbf{m}_{oct}$, which can be easily rotated by the magnetic field as demonstrated previously in bulk crystals[42,43]. Here K_1 is the anisotropy energy coefficient for sublattice moments[28,30]. In our experiment, the R_H^{ω}-β curve in the easy configuration (blue circles in Fig. 3a) deviates from a pure sinusoidal function, indicating the existence of additional anisotropies that tilt $\mathbf{m}_{oct}$ away from the applied field. To reveal these effective anisotropies, we calculate the work per unit volume done by the rotating field as measured in Fig. 3a, $\Delta E(\varphi_{oct}) \approx \mu_0 M_{net} H \int_0^{\varphi_{oct}} \sin(\beta - \varphi'_{oct}) d\varphi'_{oct}$ with μ_0 being the vacuum permeability, M_{net} representing the spontaneous (remanent) net magnetization and φ_{oct} determined

https://doi.org/10.1038/s41563-023-01620-2

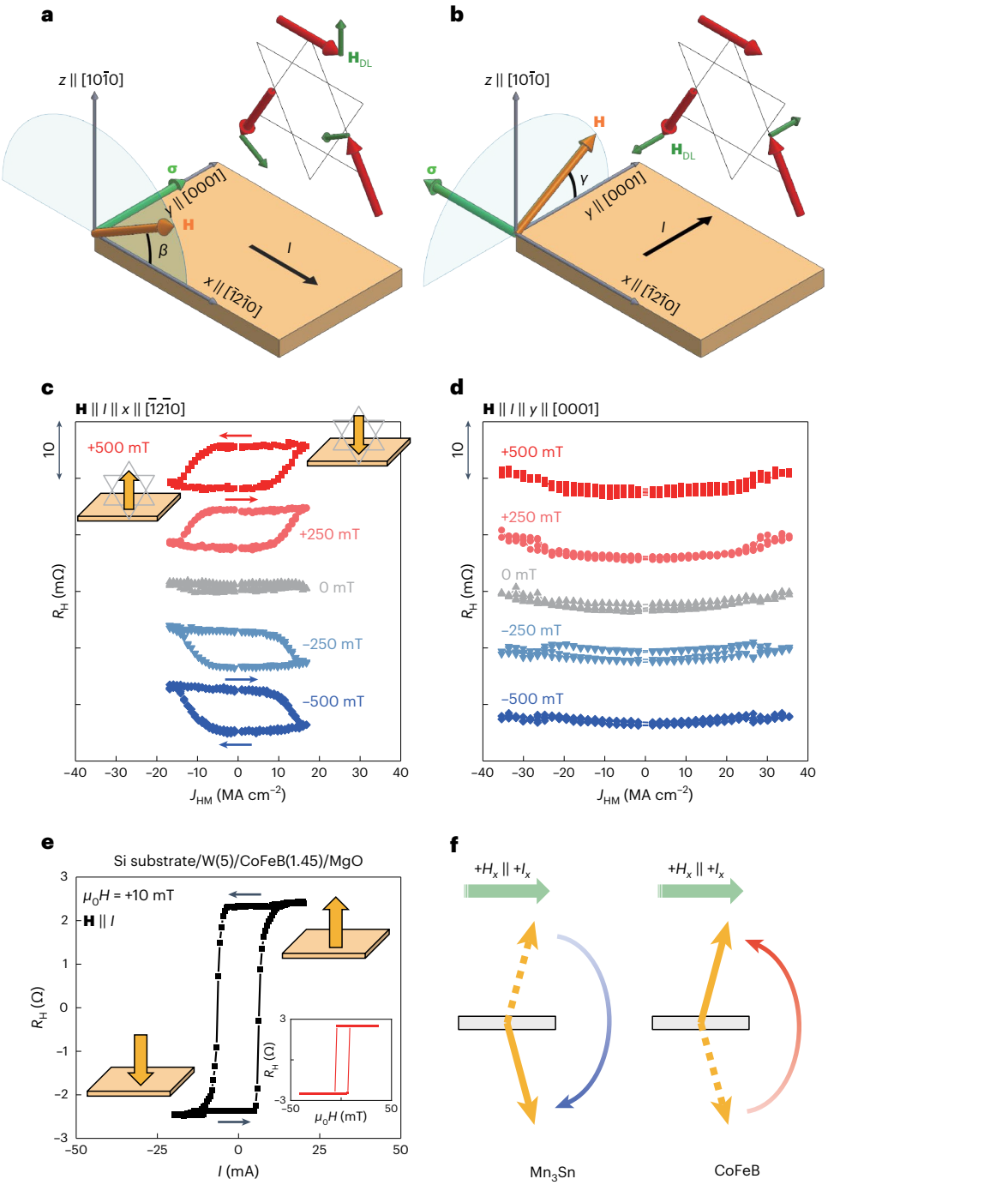

Fig. 2 | Measurement configurations and SOT switching. a,**b**, Schematics of the measurement geometry where injected spins **σ** are perpendicular (**a**) or horizontal (**b**) to the magnetic easy plane. The DL SOT effective fields of the individual sublattice moments $\mathbf{H}_{DL}$ (green arrows) and the external field **H** (orange arrow) are oriented within the easy plane (easy configuration) in **a** and out of the easy plane (hard configuration) in **b**. **c**,**d**, R_H–I curves for the easy configuration (**c**) and hard configuration (**d**), where an external field is applied along the current direction. **e**, The R_H–I curve measured in W(5 nm)/CoFeB(1.45 nm)/MgO stacks deposited on a Si substrate, where the bottom W layer injects spins with the same polarization onto the CoFeB layer as those from the top Pt layer onto the Mn_3Sn layer. The inset shows R_H as a function of the out-of-plane field, which has an opposite sign from that for Mn_3Sn. The schematics in **c** and **e** illustrate the switched magnetic states, represented by the octupole moment and the magnetization vector, respectively, in a non-collinear antiferromagnet Mn_3Sn and a ferromagnet CoFeB, respectively. We have also verified that Ru/Co/Pt, consisting of Pt as a capping layer instead of W as an underlayer, shows the same switching polarity as that of W/CoFeB/MgO. **f**, Schematic of the SOT switching of the octupole moment and the magnetization vector in Mn_3Sn and CoFeB, respectively, under the same condition of $+H_x \parallel +I_x$. The dashed and solid yellow arrows represent the initial and final states, respectively, of the order parameters.

by the measured R_H via $R_H = R_0 \sin\varphi_{oct}$. The obtained normalized $\Delta E(\varphi_{oct})$ is plotted in Fig. 3b, clearly showing that our Mn_3Sn is dominated by a twofold anisotropy with an easy axis along z, plus a fourfold anisotropy with the easy axes along ±45° and ±135°, in the form of $E_{an2} = \lambda_1 \cos(2\varphi_{oct}) + \lambda_2 \cos(4\varphi_{oct})$ where λ_1 and λ_2 are the corresponding coefficients. Microscopically, the two- and fourfold anisotropies

https://doi.org/10.1038/s41563-023-01620-2

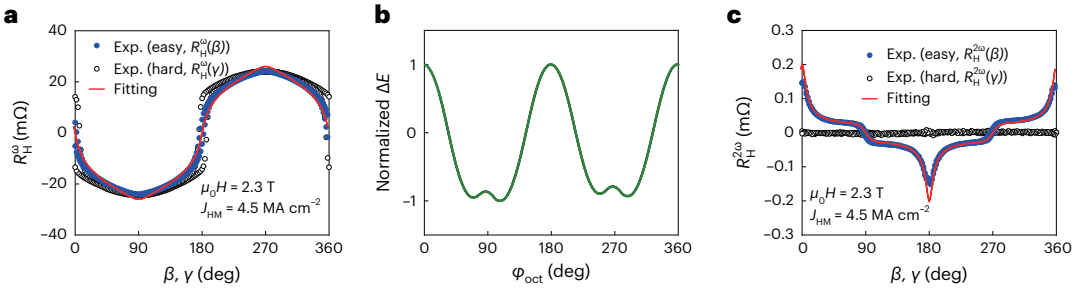

Fig. 3 | Harmonic Hall measurements and magnetic energy landscape. **a**, First-harmonic Hall resistance R_H^{ω} as a function of β and γ measured in the easy and hard configurations, respectively. Exp., experiment. **b**, The normalized ΔE–φ_{oct} curve extracted using the experimental data from **a**. **c**, Second-harmonic Hall resistance $R_H^{2\omega}$ as a function of β and γ measured in the easy and hard configuration, respectively. The red solid lines in **a** and **c** denote the fitted results of the R_H^{ω}-β and $R_H^{2\omega}$-β curves with the same fitting parameters λ_1 and λ_2.

for $\mathbf{m}_{oct}$ can be derived from the variations of the exchange interaction and the magnetocrystalline anisotropy, respectively, due to the growth-induced strain (Fig. 1d, and Supplementary Discussions 1.1, 1.2 and 4). In addition, the step-like shape of the R_H^{ω}-γ curve in the hard configuration (black circles in Fig. 3a) indicates the strong easy-plane anisotropy of the (0001) plane.

The competition between the anisotropy energies, the Zeeman energy, the exchange interactions and the Dzyaloshinskii–Moriya interaction[27–29] determines the equilibrium orientations of the three sublattice moments $\mathbf{m}_{(A,B,C)}$ and $\mathbf{m}_{oct}$. Under a given magnetic field $\mathbf{H}$, the relative orientations of the sublattice moments at equilibrium can be determined by minimizing the total energy using the perturbation method (Supplementary Discussion 1.2). The φ_{oct}-dependent magnetic energy can be described as follows, including the Zeeman term and the anisotropy terms:

$$\begin{aligned} F &\approx -\mu_0 M_0 \mathbf{m}_{net}\cdot\mathbf{H} + \lambda_1\cos(2\varphi_{oct}) + \lambda_2\cos(4\varphi_{oct}) \\ &= -\mu_0 M_0 H\left[\frac{K_1}{J}\cos(\beta-\varphi_{oct}) - \frac{\lambda_1}{K_1}\cos(\beta+\varphi_{oct})\right. \\ &\quad \left. - \frac{\lambda_2}{K_1}\cos(\beta+3\varphi_{oct})\right] + \lambda_1\cos(2\varphi_{oct}) \\ &\quad + \lambda_2\cos(4\varphi_{oct}), \end{aligned} \tag{1}$$

where J and M_0 are the exchange coefficient and the magnetization of a sublattice moment, respectively. The equilibrium octupole moment angle φ_{oct} as reflected in Fig. 3a can be determined by minimizing the energy in equation (1). With the reported values[14,18,29,30] of $\mu_0 M_0 = 0.56\,\mathrm{T}$, $K_1 = 6.7\times10^5\,\mathrm{J\,m^{-3}}$ and $J = 1.0\times10^8\,\mathrm{J\,m^{-3}}$, the measured $R_H^{\omega}(\beta)$ in the easy configuration can be well fitted by our model (the red solid line of Fig. 3a), through which $\lambda_1 = 1.7\times10^2\,\mathrm{J\,m^{-3}}$ and $\lambda_2 = 1.0\times10^2\,\mathrm{J\,m^{-3}}$ are extracted. Besides the shown example of $\mu_0 H = 2.3\,\mathrm{T}$, the R_H^{ω}-β curves under different H can all be universally fitted with the same λ_1 and λ_2 (Supplementary Fig. 6a).

Handedness and magnitude of the SOT acting on Mn_3Sn

With the equilibrium magnetic configuration determined, we now discuss the influence of SOT on the antiferromagnet dynamics. In the easy configuration, the applied current I injects spins perpendicular to the kagome plane, inducing $\mathbf{H}_{DL}^{(A,B,C)}$ onto each sublattice moment and rotating them coherently. The resulting rotation of the octupole moment $\Delta\varphi_{oct}$ can then be monitored via the change of R_H. Similar to the method widely used in studies on ferromagnets, we use the second-harmonic measurement to track the intermediate states of the octupole moment during its rotation and quantify the SOT efficiency in our Mn_3Sn/Pt samples. The mixture of the applied a.c. current and the oscillatory R_H leads to a second-harmonic resistance $R_H^{2\omega} = \frac{1}{2}\left.\frac{dR_H}{d\varphi_{oct}}\right|_{I=0}\Delta\varphi_{oct}(I)$, where I is the a.c. peak current. As shown in Fig. 3c, we see large peaks developed in $R_H^{2\omega}(\beta)$ in the easy configuration, particularly around angles corresponding to the hard axes of $\mathbf{m}_{oct}$ within the kagome plane (that is, $\varphi_{oct} = 0$ and 180°). In contrast, $R_H^{2\omega}(\gamma)$ remains tiny throughout the entire range of γ in the hard configuration (black circles in Fig. 3c), in agreement with the absence of SOT switching in Fig. 2d.

In $R_H^{2\omega}$ the SOT-induced octupole rotation $\Delta\varphi_{oct}(I)$ can be calculated via the torque balance equation $\tau_M^{oct} + \tau_{DL}^{oct}(I) = 0$, where $\tau_M^{oct}(\Delta\varphi_{oct}) = \frac{\gamma_g}{3M_0}\left.\frac{\partial^2 F}{\partial\varphi_{oct}^2}\right|_{I=0}\Delta\varphi_{oct}$ is the torque from the magnetic energy with the gyromagnetic ratio γ_g. For the DL torque $\boldsymbol{\tau}_{DL}^{oct}$ on the octupole moment, it is tempting to follow the convention developed for ferromagnets and write it as $\boldsymbol{\tau}_{DL}^{oct} = -\gamma_g\mu_0\mathbf{m}_{oct}\times\mathbf{H}_{DL}^{oct}$ with $\mathbf{H}_{DL}^{oct}\propto\mathbf{m}_{oct}\times\boldsymbol{\sigma}$ representing the SOT effective field. However, the polarity of our measured $R_H^{2\omega}$, which reflects the sign of $\Delta\varphi_{oct}$, unambiguously determines that $\mathbf{H}_{DL}^{oct} = -H_{DL}\mathbf{m}_{oct}\times\boldsymbol{\sigma}$. Here, the additional minus sign represents the fact that the octupole moment rotates in the opposite direction to the individual moments, that is, the handedness anomaly (see a detailed analysis in Supplementary Discussion 1.3). H_{DL} is the magnitude of the SOT effective field that appears in the torque on each individual sublattice moment $\mathbf{H}_{DL}^{(A,B,C)} = H_{DL}\mathbf{m}_{(A,B,C)}\times\boldsymbol{\sigma}$, with $H_{DL} = \frac{\hbar\xi_{DL}J_{HM}}{2e\mu_0(3M_0)t}$, where $\hbar$, e, ξ_{DL}, J_{HM} and t are the reduced Planck constant, the electron charge, the DL torque efficiency, the charge current density in the Pt layer and the thickness of Mn_3Sn, respectively. By solving the torque balancing equation and determining $\left.\frac{dR_H}{d\varphi_{oct}}\right|_{I=0}$ with the theoretical curve of R_H^{ω} from Fig. 3a, we plot the theoretical curve for $R_H^{2\omega}$ as the red solid line in Fig. 3c, in good agreement with the experimental results. The only free parameter in the fitting is the SOT efficiency $\xi_{DL} = 0.017$, which works universally under various applied field strengths (Supplementary Fig. 6b). In addition to fitting with the analytical model, we have also conducted full macrospin simulations by solving the coupled Landau–Lifshitz–Gilbert equations for sublattice moments, which yields identical results (Supplementary Discussion 5).

Apart from the second-harmonic measurement, we also detect the current-induced octupole rotation by applying d.c. currents[33]. Under currents with the same amplitude and opposite signs, the DL torque acting on sublattice moments rotates $\mathbf{m}_{oct}$ in opposite directions, which presents as a horizontal shift of the R_H–β curve. Figure 4a shows the experimental results, where the shifting direction is consistent with the switching polarity in Fig. 2c and opposite to that in ferromagnets. The averaged $\langle\Delta\beta\rangle$ values over the range of 0–180° under different external magnetic fields are shown in Fig. 4b, which

https://doi.org/10.1038/s41563-023-01620-2

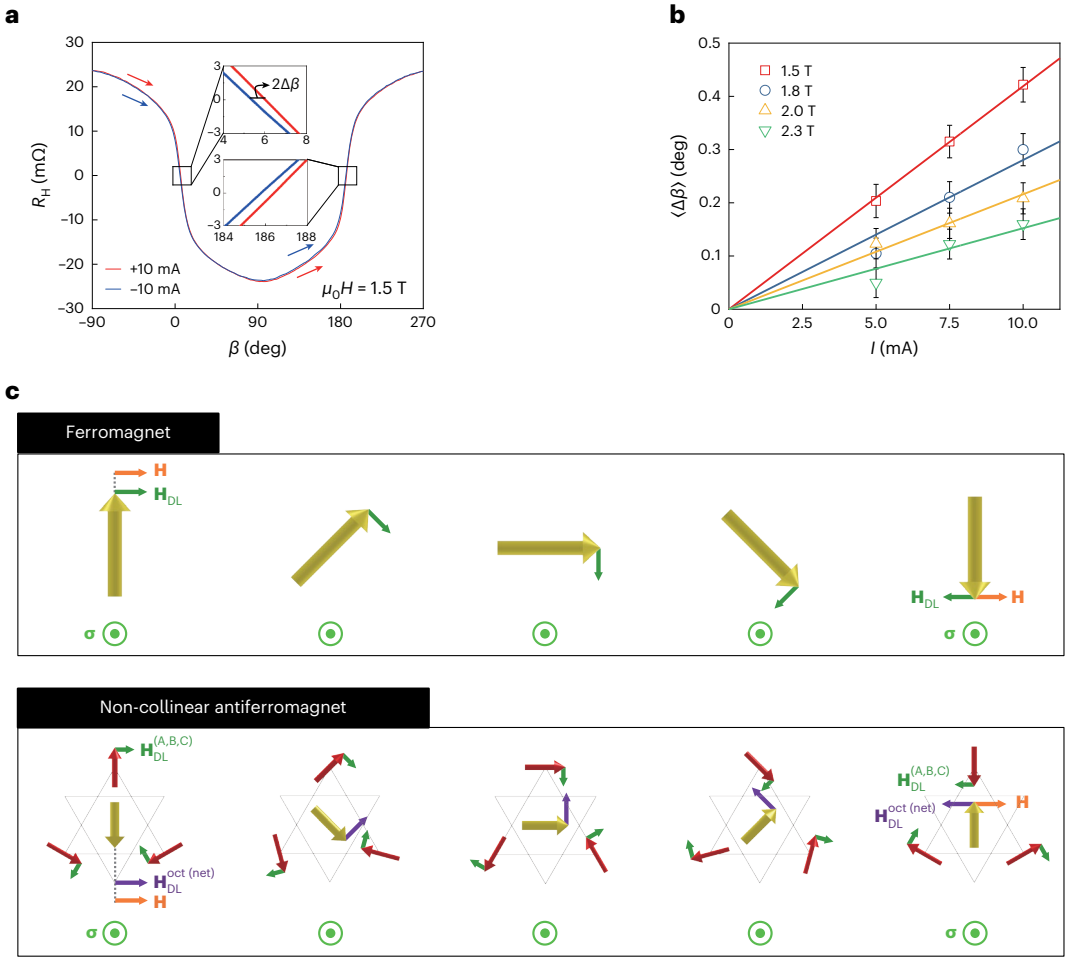

Fig. 4 | d.c. measurement and SOT switching mechanism of non-collinear antiferromagnetic order. a, R_H–β curves measured at d.c. currents of +10 and −10 mA. Insets, a magnified view to clearly show the horizontal shift $\Delta\beta$ between the two curves. **b**, Summary of $\langle\Delta\beta\rangle$ as a function of I under various magnetic fields, where the error bar is the mean absolute error of the observed data points (n = 360) using the measurement error of 0.01 mΩ. **c**, Schematics of the SOT switching mechanisms in conventional ferromagnets and non-collinear antiferromagnets. The five subfigures in each case highlight the magnetic states during a switching process, from left to right, with the right most subfigures being the final stable state. For the ferromagnet, the yellow arrow represents the magnetization vector. For the non-collinear antiferromagnet, sublattice moments (red arrows) and the octupole moment (yellow arrow) exhibit opposite handedness under the SOT. The orientations of the DL effective field on the sublattice moments and the octupole moment (as well as the net moment) are illustrated as green and purple arrows, respectively.

indicates the linear relationship between the DL effective field and the applied current. Accordingly, a SOT efficiency of $\xi_{DL} = 0.017 \pm 0.004$ is extracted (Supplementary Discussion 1.4), which is in good agreement with the result from the second-harmonic approach. The SOT efficiency obtained in this work is smaller than the typical spin Hall angles of Pt. This could be due to the low transparency at the Mn_3Sn/Pt interface or the complicated interactions between conduction electron spins and local moments in the presence of antiferromagnetic exchange interactions, which will be investigated in the future. In addition to the SOT from Pt, it was reported that polycrystalline Mn_3Sn can exhibit a self-torque as a result of the grain-to-grain spin transfer[44]. Given the epitaxial nature of our Mn_3Sn film, the grain-mediated self-torque picture is not applicable to our study.

Discussion

The switching of the non-collinear antiferromagnetic order shows some similarities with regular ferromagnets, including the realization of deterministic switching with applied in-plane magnetic fields. However, a simple treatment of the non-collinear antiferromagnet as a weak rigid ferromagnet by tracking its magnetization vector predicts the wrong sign for the switching polarity. To better illustrate this crucial difference, Fig. 4c conceptually compares the SOT switching between conventional ferromagnets and non-collinear antiferromagnets, where the SOT leads to opposite final orientations of the representative magnetic order parameters through the balance of the external field and the DL effective field. Our observation on the sign reversal of the SOT switching, together with the good agreement between the measured $R_H^{2\omega}$ and our analytical model, provides clear evidence that the assembled SOT effect on the sublattice moments drives $\mathbf{m}_{oct}$ to rotate in the opposite direction from the sublattice moments $\mathbf{m}_{(A,B,C)}$, causing the handedness anomaly that distinguishes the dynamics of non-collinear antiferromagnets from the classical dipole dynamics of ferromagnets. We note that the schematics shown in Fig. 4c are depicted based on a quasistatic process to easily capture the difference in the magnetic dynamics of the ferromagnet and the non-collinear antiferromagnet in the low-frequency regime, which is appropriate for interpreting our harmonic and d.c. measurements. To precisely describe the switching and chiral-spin rotation in the (sub-)nanosecond regime, one needs to further include the accompanying dynamics in the direction perpendicular to the kagome plane.

As a final remark, our harmonic and d.c. measurements consistently quantify a reasonable SOT efficiency from Pt, which is sufficient to overcome the strain-induced two- and fourfold anisotropies and

to enable the switching. This quantification, together with our estimation of a weak temperature increase in the experiments, provides useful insights into the long debate on the thermal contributions in the current-induced switching of antiferromagnets[17,45,46]. In future studies, by interface engineering, one can potentially tune the strain-induced anisotropies, which are much stronger than the intrinsic sixfold anisotropy, to reduce the switching current by at least an order of magnitude and to develop configurations with optimal anisotropy for designing antiferromagnetic nano-oscillators with continuous chiral-spin rotations[14].

Online content

Any methods, additional references, Nature Portfolio reporting summaries, source data, extended data, supplementary information, acknowledgements, peer review information; details of author contributions and competing interests; and statements of data and code availability are available at https://doi.org/10.1038/s41563-023-01620-2.

References

1. Jungwirth, T., Marti, X., Wadley, P. & Wunderlich, J. Antiferromagnetic spintronics. *Nat. Nanotechnol.* **11**, 231–241 (2016).
2. Baltz, V. et al. Antiferromagnetic spintronics. *Rev. Mod. Phys.* **90**, 015005 (2018).
3. Železný, J., Wadley, P., Olejník, K., Hoffmann, A. & Ohno, H. Spin transport and spin torque in antiferromagnetic devices. *Nat. Phys.* **14**, 220–228 (2018).
4. Wadley, P. et al. Electrical switching of an antiferromagnet. *Science* **351**, 587–590 (2016).
5. Nakatsuji, S., Kiyohara, N. & Higo, T. Large anomalous Hall effect in a non-collinear antiferromagnet at room temperature. *Nature* **527**, 212–215 (2015).
6. Higo, T. et al. Anomalous Hall effect in thin films of the Weyl antiferromagnet Mn_3Sn. *Appl. Phys. Lett.* **113**, 202402 (2018).
7. Ikeda, T. et al. Anomalous Hall effect in polycrystalline Mn_3Sn thin films. *Appl. Phys. Lett.* **113**, 222405 (2018).
8. Ikhlas, M. et al. Large anomalous Nernst effect at room temperature in a chiral antiferromagnet. *Nat. Phys.* **13**, 1085–1090 (2017).
9. Higo, T. et al. Large magneto-optical Kerr effect and imaging of magnetic octupole domains in an antiferromagnetic metal. *Nat. Photon.* **12**, 73–78 (2018).
10. Uchimura, T. et al. Observation of domain structure in non-collinear antiferromagnetic Mn_3Sn thin films by magneto-optical Kerr effect. *Appl. Phys. Lett.* **120**, 172405 (2022).
11. Manchon, A. et al. Current-induced spin-orbit torques in ferromagnetic and antiferromagnetic systems. *Rev. Mod. Phys.* **91**, 035004 (2019).
12. Shao, Q. et al. Roadmap of spin–orbit torques. *IEEE Trans. Magn.* **57**, 1–39 (2021).
13. Ryu, J., Lee, S., Lee, K.-J. & Park, B.-G. Current-induced spin–orbit torques for spintronic applications. *Adv. Mater.* **32**, 1907148 (2020).
14. Takeuchi, Y. et al. Chiral-spin rotation of non-collinear antiferromagnet by spin–orbit torque. *Nat. Mater.* **20**, 1364–1370 (2021).
15. Yan, G. Q. et al. Quantum sensing and imaging of spin–orbit-torque-driven spin dynamics in the non-collinear antiferromagnet Mn_3Sn. *Adv. Mater.* **34**, 2200327 (2022).
16. Tsai, H. et al. Electrical manipulation of a topological antiferromagnetic state. *Nature* **580**, 608–613 (2020).
17. Pal, B. et al. Setting of the magnetic structure of chiral kagome antiferromagnets by a seeded spin-orbit torque. *Sci. Adv.* **8**, eabo5930 (2022).
18. Higo, T. et al. Perpendicular full switching of chiral antiferromagnetic order by current. *Nature* **607**, 474–479 (2022).
19. Krishnaswamy, G. K. et al. Time-dependent multistate switching of topological antiferromagnetic order in Mn_3Sn. *Phys. Rev. Appl.* **18**, 024064 (2022).
20. Suzuki, M.-T., Koretsune, T., Ochi, M. & Arita, R. Cluster multipole theory for anomalous Hall effect in antiferromagnets. *Phys. Rev. B* **95**, 094406 (2017).
21. Nomoto, T. & Arita, R. Cluster multipole dynamics in noncollinear antiferromagnets. *Phys. Rev. Res.* **2**, 012045 (2020).
22. Liu, L., Moriyama, T., Ralph, D. C. & Buhrman, R. A. Spin-torque ferromagnetic resonance induced by the spin Hall effect. *Phys. Rev. Lett.* **106**, 036601 (2011).
23. Finley, J. & Liu, L. Spintronics with compensated ferrimagnets. *Appl. Phys. Lett.* **116**, 110501 (2020).
24. Kim, S. K. et al. Ferrimagnetic spintronics. *Nat. Mater.* **21**, 24–34 (2022).
25. Cheng, R., Xiao, J., Niu, Q. & Brataas, A. Spin pumping and spin-transfer torques in antiferromagnets. *Phys. Rev. Lett.* **113**, 057601 (2014).
26. Chen, X. Z. et al. Antidamping-torque-induced switching in biaxial antiferromagnetic insulators. *Phys. Rev. Lett.* **120**, 207204 (2018).
27. Nagamiya, T., Tomiyoshi, S. & Yamaguchi, Y. Triangular spin configuration and weak ferromagnetism of Mn_3Sn and Mn_3Ge. *Solid State Commun.* **42**, 385–388 (1982).
28. Tomiyoshi, S. & Yamaguchi, Y. Magnetic structure and weak ferromagnetism of Mn_3Sn studied by polarized neutron diffraction. *J. Phys. Soc. Jpn.* **51**, 2478–2486 (1982).
29. Cable, J. W., Wakabayashi, N. & Radhakrishna, P. Magnetic excitations in the triangular antiferromagnets Mn_3Sn and Mn_3Ge. *Phys. Rev. B* **48**, 6159–6166 (1993).
30. Sandratskii, L. M. & Kübler, J. Role of orbital polarization in weak ferromagnetism. *Phys. Rev. Lett.* **76**, 4963–4966 (1996).
31. Yoon, J. et al. Crystal orientation and anomalous Hall effect of sputter-deposited non-collinear antiferromagnetic Mn_3Sn thin films. *Appl. Phys. Express* **13**, 013001 (2019).
32. Yoon, J.-Y. et al. Correlation of anomalous Hall effect with structural parameters and magnetic ordering in $Mn_{3+x}Sn_{1-x}$ thin films. *AIP Adv.* **11**, 065318 (2021).
33. Zhang, P. et al. Control of Néel vector with spin-orbit torques in an antiferromagnetic insulator with tilted easy plane. *Phys. Rev. Lett.* **129**, 017203 (2022).
34. Yamane, Y., Gomonay, O. & Sinova, J. Dynamics of noncollinear antiferromagnetic textures driven by spin current injection. *Phys. Rev. B* **100**, 054415 (2019).
35. Chen, H., Niu, Q. & MacDonald, A. H. Anomalous Hall effect arising from noncollinear antiferromagnetism. *Phys. Rev. Lett.* **112**, 017205 (2014).
36. Yang, H. et al. Topological Weyl semimetals in the chiral antiferromagnetic materials Mn_3Ge and Mn_3Sn. *N. J. Phys.* **19**, 015008 (2017).
37. Pai, C.-F. et al. Spin transfer torque devices utilizing the giant spin Hall effect of tungsten. *Appl. Phys. Lett.* **101**, 122404 (2012).
38. Miron, I. M. et al. Perpendicular switching of a single ferromagnetic layer induced by in-plane current injection. *Nature* **476**, 189–193 (2011).
39. Liu, L., Lee, O. J., Gudmundsen, T. J., Ralph, D. C. & Buhrman, R. A. Current-induced switching of perpendicularly magnetized magnetic layers using spin torque from the spin Hall effect. *Phys. Rev. Lett.* **109**, 096602 (2012).
40. Pi, U. H. et al. Tilting of the spin orientation induced by Rashba effect in ferromagnetic metal layer. *Appl. Phys. Lett.* **97**, 162507 (2010).

41. Han, J. et al. Room-temperature spin-orbit torque switching induced by a topological insulator. *Phys. Rev. Lett.* **119**, 077702 (2017).
42. Duan, T. F. et al. Magnetic anisotropy of single-crystalline Mn_3Sn in triangular and helix-phase states. *Appl. Phys. Lett.* **107**, 082403 (2015).
43. Liu, J. & Balents, L. Anomalous Hall effect and topological defects in antiferromagnetic Weyl semimetals: Mn_3Sn/Ge. *Phys. Rev. Lett.* **119**, 087202 (2017).
44. Xie, H. et al. Magnetization switching in polycrystalline Mn_3Sn thin film induced by self-generated spin-polarized current. *Nat. Commun.* **13**, 5744 (2022).
45. Chiang, C. C., Huang, S. Y., Qu, D., Wu, P. H. & Chien, C. L. Absence of evidence of electrical switching of the antiferromagnetic Néel vector. *Phys. Rev. Lett.* **123**, 227203 (2019).
46. Zhang, P., Finley, J., Safi, T. & Liu, L. Quantitative study on current-induced effect in an antiferromagnet insulator/Pt bilayer film. *Phys. Rev. Lett.* **123**, 247206 (2019).

Methods

Sample preparation

Stacks with W(2 nm)/Ta(3 nm)/Mn_3Sn(30 nm)/MgO(1.3 nm)/Ru(1 nm) were deposited by d.c. and radio-frequency magnetron sputtering on a MgO(110) single-crystal substrate. W, Ta, Mn_3Sn and Ru were deposited at 400 °C and MgO was deposited at room temperature. The deposition was implemented under a base pressure of less than 1×10^{-6} Pa. After deposition, samples were annealed at 600 °C for 1 hour in vacuum. After annealing, capping layers (MgO/Ru) and part of the Mn_3Sn layer were etched by Ar ion milling. The thickness of the remaining Mn_3Sn layer was obtained as 8.8 nm by X-ray reflectivity measurements. After etching, the Pt(5 nm) layer was deposited on top of the Mn_3Sn layer. Before deposition of the Pt layer, the surface of Mn_3Sn was etched by bias sputtering for 20 s to remove any oxides that might be formed in the process of moving the samples from the Ar ion milling chamber to the sputtering chamber. The samples were fabricated onto a Hall bar structure by photolithography. Two different channel widths W_{ch} of 30 μm and 15 μm were employed to apply small and large current densities, respectively. The channel length L_{ch} and probe width were 90 μm and 8 μm, respectively. Electrodes consisting of Ta(5 nm)/Ru(50 nm)/Pt(5 nm) were deposited by d.c. sputtering and fabricated into square shape contact pads by photolithography and lift-off.

X-ray diffraction

A Cu Kα1 X-ray with a wavelength of 1.54056 Å was used in our X-ray diffraction measurements. 2θ–θ scan and ϕ scan measurements were performed using a Bruker X-ray diffractometer. Reciprocal space mapping measurements were performed using a X'Pert^3 Materials Research Diffractometer, where the two-dimensional data were collected using a two-dimensional solid-state hybrid pixel detector.

Transport measurements

The transport measurements were performed on Hall bar devices with a four-probe method as shown in Fig. 1e. The d.c. and a.c. currents were applied up to 10 mA in all of our transport measurements except for the d.c. pulse measurement. The 47.311 Hz a.c. current was applied with an EG&G DSP 7260 Lock-in Amplifier, and d.c. current was applied with a Keithley 2400 current source, which is designed for at most kilohertz sourcing. The harmonic Hall measurement was performed by a lock-in technique. The resistivities of each layer in the stacks were obtained from sheet resistance measurements of the blanket films with various thicknesses, where the growth conditions were consistent with the samples used for the transport measurements. The resistivities of the W, Ta, Mn_3Sn and Pt layers were calibrated as 60.2, 122.8, 333.3 and 29.0 μΩ cm, respectively. The current density of the heavy metal was calculated considering the current distribution of each layer following a parallel resistance model. The percentages of current flowing in the W, Ta, Mn_3Sn and Pt layers were obtained as 13.0%, 9.5%, 10.3% and 67.2%, respectively. From the current distribution calculation, we found that a seven times larger current flows in the Pt layer than in the Ta layer, and the current density in the Pt layer is four times larger than that in the Ta layer. Since most of the current flows in Pt rather than Ta, we only considered Pt as the heavy metal layer adjacent to the Mn_3Sn layer for the simplicity of our analysis.

Calculation and analysis

The numerical computing software MATLAB was used for the fitting of harmonic measurements. We performed a series expansion with the help of Mathematica in the perturbation method calculations.

Data availability

The data that support the findings of this study are available within the Article and its Supplementary Information. Source data are provided with this paper.

Code availability

The calculation and simulation codes are available from the corresponding authors.

Acknowledgements

We thank J. Ieda, B. Jinnai, J. Llandro, Y. Yamane, K. Kishi and Y. Sato for their technical support and fruitful discussions. Reciprocal space mapping was performed at the Fundamental Technology Center of RIEC in Tohoku University with technical support from T. Tanno. This work was supported by the JSPS Kakenhi (grant nos. 19H05622, 21J23061, 22F32037 and 22K14558), Iketani Science and Technology Foundation (grant no. 0331108-A), Casio Science and Technology Foundation (grant nos. 39-11 and 40-4), Research Institute of Electrical Communication Cooperative Research Projects, National Science Foundation under award no. DMR-2104912 and Semiconductor Research Corporation. J.-Y.Y. and T.U. acknowledge support from GP-Spin at Tohoku University. P.Z. acknowledges support from the Mathworks Fellowship. J.H. acknowledges support from the JSPS Postdoctoral Fellowship for Research in Japan.

Author contributions

J.-Y.Y., P.Z., J.H., H.O., S.F. and L.L. planned the study. J.-Y.Y., Y.T. and T.U. prepared the samples with guidance from S.F. J.-Y.Y., P.Z., C.-T.C. and J.T.H. fabricated the films into Hall bar devices and set the samples for transport measurements. J.-Y.Y. and P.Z. performed transport measurements and analysed the data with advice from Y.T., J.H., S.F. and L.L. J.-Y.Y. and C.-T.C. performed the X-ray diffraction and analysed the structural properties of Mn_3Sn. P.Z. performed the theoretical calculation with input from J.-Y.Y. and L.L. J.H. and L.L. conceptualized the findings with input from S.F. All authors discussed the results. J.-Y.Y., P.Z., J.H. and L.L. wrote the manuscript with input from S.F. L.L. supervised the research.

Competing interests

The authors declare no competing interests.

Additional information

Supplementary information The online version contains supplementary material available at https://doi.org/10.1038/s41563-023-01620-2.

Correspondence and requests for materials should be addressed to Jiahao Han, Shunsuke Fukami or Luqiao Liu.

Peer review information *Nature Materials* thanks Andrew Kent and the other, anonymous, reviewer(s) for their contribution to the peer review of this work.